Evaluation of General Resistivity Density-Based Saturation in Thin, Laminated Sand-Shale Sequences*

John Quirein[1], Burkay Donderici[1], David Torres[1], Eric Murphy[1], and Jim Witkowsky[1]

Search and Discovery Article #41042 (2012)*
Posted October 22, 2012

*Adapted from extended abstract prepared in conjunction with oral presentation at AAPG International Convention and Exhibition, Singapore, 16-19 September 2012, AAPG©2012

[1]Halliburton, Houston, TX (john.quirein@halliburton.com)

Abstract

Thin, laminated sand-shale sequences can occur in all kinds of depositional environments, such as fluvial point bars, deltas, deepwater submarine fans, and turbidites and can trap significant amounts of hydrocarbons in the thin, sandy beds. Evaluation with conventional low-resolution uniaxial resistivity tools of the electrically anisotropic sand-shale sequences may result in significant underestimation of the hydrocarbon pore volume in the reservoir. A triaxial multicomponent induction tool can be used to characterize the electrical anisotropy in terms of the horizontal and vertical components of the formation resistivity. An interpretation model can be applied to convert the measured horizontal and vertical resistivities into the sand resistivity and sand volume. With the proper analysis, this translates into an enhanced hydrocarbon recovery and optimized reservoir development.

This paper provides a complete rock model and a comprehensive workflow that takes into account all the necessary stages to estimate water saturation in a thinly bedded sand-shale sequence, where both laminated and dispersed shale types can exist. It is shown that the Thomas-Stieber model can be applied, in conjunction with an approximation of total porosity, to compute the sand total and effective porosity. This allows net-pay cutoffs to be applied based on sand volume, porosity, and water saturation. Different clay-bound water sources will be assumed. If grain density information is available from sources, like downhole geochemical logging tools or well site energy-dispersive x-ray fluorescence, the process can be made more accurate by iteratively solving for porosity and saturation from the bulk density along with the horizontal and vertical resistivity measurements. This is accomplished by applying a robust and efficient nonlinear solver, which has been built to take into account the possible dependence of the fluid density on the saturation, as well as the dependence of the saturation and cementation exponents (N and M) on the total porosity.

Several field examples are presented for both wireline and LWD measurements. Dispersed shale is interpreted using any of the Dual-Water, Simandoux, and Indonesia equations.

Laminated Sand-Shale Sequences Interpretation Models

Thin laminated sand-shale sequences can occur in all kinds of depositional environments, such as fluvial point bars, deltas, deepwater submarine fans, and turbidites and can trap significant amounts of hydrocarbons in the thin, sandy beds. Resistivity anisotropy occurs from alternating thin beds or laminations of differing resistivity, where the individual bed thicknesses are less than the resolution of the resistivity tools (Klein 1993), and this kind of anisotropy is often called "macroscopic anisotropy". In some stratified rocks, some grains possess a flat or elongated shape (e.g., mica and illite) and were laid down with an orientation parallel to the sedimentation strata at the time of deposition by nature and are often categorized as shale. Electric currents have a preferred path parallel to the bedding compared to perpendicular to the bedding, and this kind of anisotropy is referred to as "microscopic anisotropy" (Yin et al. 2008).

Yin et al. 2008 provides a good overview of many published resistivity anisotropy models prior to 2008. These models generally describe an effective resistivity anisotropy (macro anisotropy) resulting from the horizontal and vertical resistivities that are derived from tool measurements. Some of the models consider the intrinsic microscopic anisotropy of the shales. Note the industry convention is to use the notation, R_h, for the "horizontal" and R_v for the "vertical" resistivity, where, in reality, R_h is the derived resistivity parallel to the bedding, and R_v is the derived resistivity perpendicular to the bedding, as illustrated by Figure 1.

A simple example is presented to illustrate the effect of macro anisotropy on the horizontal and vertical resistivities derived from simulated tool measurements. In this simple example, we assume no dip and no shale micro anisotropy. In Figure 2, Track 1 displays the physical model, where dark brown represents shale and tan represents sand. Track 2 shows that the upper sand has a resistivity of about 80 Ω-m, whereas the other sands have a true resistivity of 20 Ω-m. The shale is isotropic, with a resistivity of 1 Ω-m. For this particular example, it can be seen that in laminated beds, R_h is close to the shale resistivity, R_{shale}, and R_v is close to, but less than, the sand resistivity, R_{sand}. From an interpretation point of view, we are interested in the sand resistivity, R_{sand}, and sand volumetric fraction, V_{sand}, but these cannot be measured and must be derived using an interpretation model. All current models for doing this (Mollison et al. 2001 and Hayden et al. 2009) and allowing for shale microscopic anisotropy are generally of the form:

$$R_v = R_{sand}(1 - V_{lam}) + R_{shale\_vertical} V_{lam} \tag{1}$$

$$\frac{1}{R_h} = \frac{(1 - V_{lam})}{R_{sand}} + \frac{V_{lam}}{R_{shale\_horizontal}} \tag{2}$$

$$1 = V_{lam} + V_{sand} \tag{3}$$

The most common implementation of Eqs. 1–3 are to obtain R_v and R_h derived from tool measurements, input parameters, $R_{shale\_vertical}$ and $R_{shale\_horizontal}$, generally selected from observing R_v and R_h in the neighboring shale, and then solving for the sand resistivity, R_{sand}, and volumetric fraction laminated shale, V_{lam}. Note that it is possible for sand volumetric fraction, V_{sand}, to contain some dispersed shale, as discussed by Thomas and Stieber 1975.

Figure 3a, Figure 3b and Figure 3c plot the R_v and R_h of Eqs. 1–2 for various values of R_{sand}, $R_{shale\_vertical}$, and $R_{shale\_horizontal}$. Figure 3a illustrates macro anisotropy when both the sand and shale are isotropic. Figure 3b illustrates when the shale micro anisotropy is small (ratio of shale vertical to horizontal resistivity is 2). The macro anisotropy (R_v/R_h ratio depicted by green curve) is similar to the macro anisotropy of the isotropic shale model of Figure 3a. Figure 3c illustrates the case where the shale micro anisotropy is high (ratio of shale vertical to horizontal resistivity is 10). It is noted for all three cases that the horizontal resistivity, R_h, remains constant.

Porosity and Net-Pay for Laminated Sand-Shale Sequences Interpretation Models

In the previous section, we discussed how the sand resistivity, R_{sand}, and volumetric fraction laminated shale, V_{lam}, could be obtained. However, we are interested in the hydrocarbon saturation within the sand, and to accomplish this, we need to predict the sand porosity. Again, the general approach for doing this (Mollison et al. 2001 and Hayden et al. 2009) is to use the following equation:

$$\phi_{t\_sd} = \frac{\phi_t - V_{lam}\phi_{sh}}{(1 - V_{lam})} \tag{4}$$

Where, the total porosity is ϕ_t, the shale porosity is ϕ_{sh}, and the sand total porosity is ϕ_{t_sd}, so that it is possible that the sand contains some dispersed shale/clay. Eq. 4 is a particular representation of one form of the Thomas-Stieber model, and if the total shale volumetric fraction, V_{sh}, is available from another source (from gamma ray, etc), the solution from Eq. 4 is represented by the dashed red line of Figure 4, obtained from Yared et al. 2010.

To simplify the following discussion, we assume that there is no dispersed shale; therefore, in this case, Eq. 4 becomes:

$$\phi_{e\_sd} = \phi_{t\_sd} = \phi_{\max} = \frac{\phi_t - V_{lam}\phi_{sh}}{(1 - V_{lam})} = \frac{\phi_e}{V_{sand}} \tag{5}$$

so that the sand effective porosity, ϕ_{e_sd}, is always greater than the effective porosity, ϕ_e, of the rock (laminated sand-shale sequence), and if the sand effective porosity, ϕ_{e_sd}, is 30 pu but the volumetric sand fraction is .5, the resulting effective porosity, ϕ_e, will be 15 pu. Thus, a net-pay flag dependent on ϕ_e can be expected to find less pay then that found with a net-pay flag dependent upon ϕ_{e_sd}, even though the volume of the hydrocarbon in the formation is the same for both cases. Similarly, use of the formation total water saturation, S_{wt}, for computation of the net-pay flag will be more pessimistic than a net-pay flag dependent on the sand total water saturation, $S_{wt\text{-}sand}$.

When there is dispersed shale, it can be computed independent from the Thomas-Stieber model from the difference of the total volume shale and the volume-laminated shale, as illustrated in Figure 4:

$$V_{disp} = V_{sh} - V_{lam} \tag{6}$$

The Thomas-Stieber model can be used to impose a physical constraint that the volume of dispersed shale must be less than the maximum clean sand porosity, ϕ_{max}. Figure 5 compares the Thomas-Stieber interpretation with the resistivity anisotropy-based interpretation. When there is zero dip, R_t is equal to R_h; thus, from Eq. 2, both interpretations are equivalent (as long as the volume of laminated shale from both models agree), as R_{sand} can be obtained. The strength of the resistivity anisotropic interpretation is that it compensates for dip.

Extending the Thomas-Stieber Model in the Presence of Dip Closer to the Electrical Anisotropic Model

Moran and Gianzero (1979) studied the effects of formation anisotropy on resistivity logging measurements. In a homogeneous, infinitely thick anisotropic formation, both induction and laterolog resistivity tools (R_{log}) will respond to borehole deviation (or relative, formation to borehole, *dip*), vertical resistivity, R_v, and horizontal resistivity, R_h:

$$R_{\log} = \frac{\lambda R_h}{\sqrt{\sin^2\alpha + \lambda^2 \cos^2\alpha}} \tag{7}$$

Where, α is the bed inclination (relative *dip*), and $\lambda$is the anisotropy coefficient, which is defined as:

$$\lambda^2 = \frac{R_v}{R_h} \tag{8}$$

We need to make three assumptions to eliminate the relative dip effect: 1) that relative dip is known or available from image data, 2) that we have a pure shale zone, and 3) that λ^2 is known in the pure shale. In this case, in the pure shale zone, we can determine the shale horizontal, $R_{shale\_horizontal,}$ and vertical resistivity, $R_{shale\_vertical}$:

$$R_{shale\_horizontal} = \frac{R_{\log\_shale}\sqrt{\sin^2\alpha + \lambda^2 \cos^2\alpha}}{\lambda} \tag{9}$$

$$R_{shale\_vertical} = \lambda^2 R_{shale\_horizontal} \tag{10}$$

With the parameters shale horizontal, $R_{shale\_horizontal}$, and vertical resistivity, $R_{shale\_vertical}$, known, and the laminated shale volume, V_{lam}, obtained from the Thomas-Stieber model also known, and substituting Eqs. 1 and 2 into Eq. 7, then Eq. 7 can be solved for the only remaining unknown, i.e. R_{sand}.

Figure 6 replicates Figure 3c, where the shale micro anisotropy is high (ratio of shale vertical to horizontal resistivity is 10), but, in addition, plots the response of the resistivity tool, R_{log}, as obtained from Eq. 7 for the cases 30° (Rlog-30), 60° (Rlog-60) and 90°

(Rlog-90) relative dip (or borehole deviation). It can be seen that not correcting for relative dip of 30° will result in a pessimistic interpretation, whereas, at the higher relative dips of 60 and 90°, the interpretation will be optimistic.

LWD/Wireline Tools and Their Anisotropy/Dip Sensitivities

Traditional induction-propagation resistivity logging tools (such as Halliburton EWR or ACRt) rely on an array of coaxial antennas that are disposed along the borehole axis. These tools can take advantage of the multi-spacing data to produce curves that are associated with different depths of investigation. This helps with correction of borehole and invasion effects that can lead to the true resistivity of the formation without the borehole distortion. Another class of induction-propagation resistivity logging tool includes well-placement geosteering tools (such as Halliburton ADR). These tools have azimuthally sensitive resistivity readings, which enable the determination of position and orientation of boundaries around the wellbore. Both logging and well placement tools are used to evaluate anisotropy of formations; however, they have a limitation on the minimum dip angle that they can operate with for reliable operation (determination of R_v, R_h, and *dip*) owing to the low sensitivity of the signal components used in these tools at low dip angles. Multi-component induction tools (such as Halliburton *Xaminer*™- *MCI*) are developed to reliably measure anisotropy of formations. These tools feature nine tensor components composed of three transmitter orientations and three receiver orientations. Figure 7 shows the signal components that are available in each type of tool and the percentage sensitivity of each component to R_v and *dip* as a function of dip angle. The sensitivity displayed is the sensitivity of a component divided by the sum of all components where sensitivity is defined as the change on the signal due to change in the parameter (anisotropy constant in this case).

As shown in Figure 7, traditional resistivity tools only have the ZZ component, which is sensitive to anisotropy only if the dip is larger than 70° (see the right-hand plot in Figure 7). Geosteering tools have XZ, YZ, ZX, and ZY in addition to the ZZ component, which widen the reliable anisotropy inversion range to dip above 40°. Anisotropy tools, on the other hand, are sensitive to all nine components, including XX and YY, which are maximally sensitive to anisotropy and dip around zero dip angle. As a result, anisotropy tools can reliably measure anisotropy and intrinsic dip of formations at any dip angle.

Wireline Anisotropy Tool: Xaminer™-MCI. The *Xaminer*™- *MCI* (Figure 8) has a transmitter triad (collocated triaxial array of 3 coils) and six sets of receiver coils. The two closest receiver coils to the transmitter are standard induction coils, while the remaining four coils are built as triads. The tool operates by sequentially energizing each of the coils (X, Y, Z) in the transmitter triad and measuring the signals in each of the receiver coils. Hence, each of the receiver triads produces nine signals per frequency. These signals are corrected for borehole effects and then inverted to obtain the desired formation measurements. R_h, R_v, Relative (formation

to Borehole) *Dip* and *Azimuth*. Usually the tool is run with a directional package so that true formation *Dip* and *Azimuth* can be found and is run with a six-arm caliper to find the relative position of the tool in the borehole.

The tool also provides the same logs as Halliburton's ACRt tool. To do this, the transmitter spacings are the same as the ACRt tool and, like the ACRt, it also uses three frequencies to do the Skin Effect correction. All the signals measured on the Z receivers when the transmitter is fired follow the same processing as the standard ACRt tool to match the response of the ACRt tool.

The tool operates centralized in boreholes filled with air or oil-based mud. Each receiver triad is an arrangement of six coils: three main and three bucking coils, each pair for one of the three orthogonal directions X, Y, Z and is represented diagrammatically with its equivalent dipole model in Figure 9. Both the main and bucking coils are collocated, and the bucking coils are wound as to minimize the direct coupling signals. The transmitter triad only has three main collocated coils. Each triad sends up hole a nine component complex tensor for each frequency. The tool energizes the formation with four frequencies simultaneously. All of the information from the four triads, plus the short spacing information, is converted into a digital string that is sent uphole via the telemetry system. All of these voltages are calibrated to mmh/m, and all of the signals are compensated for temperature changes in the sonde error, electronics drifts, and changes in gain. The uphole processing software calculates the tool position in the borehole and removes any effects from tool position and borehole effects. To do so, a first 1-D radial inversion algorithm is used. Because of this inversion, a first quick look of the results (R_h, R_v, dip, azimuth) can be presented in real time, and all of the borehole corrected tensors can be presented. The borehole corrected tensors are the input (post real time) to a 1-D vertical inversion algorithm. This algorithm squares the log, and the results give answers that have reduced shoulder bed effects. All the details are provided by Hou et al. 2012.

Field Log Fort Worth, Texas—Test Well Example Wireline Anisotropy Tool: Xaminer™-MCI

A prototype of the new tool was well tested in Fort Worth, Texas, and an anisotropic interpretation was performed using Eqs. 1–3 to estimate the sand resistivity and volume–laminated shale. The data in this formation is a sequence of sands and shales, but the shale has a lot of micro-anisotropy and was modeled from observation of the data with shale horizontal, $R_{shale\_horizontal} = 6$ Ω-m, and vertical resistivity, $R_{shale\_vertical} = 70$ Ω-m. Note that the interpreted results are very sensitive to these parameters when there is a lot of laminated shale, as illustrated by Figure 10 from Minh et al. 2008. In this figure, the red contours correspond to values of constant sand resistivity. Note that they all converge to a common "pure shale point". Actual data lying within the black circle will exhibit a lot of variability in the computed value for the sand resistivity, R_{sand}. The blue contours represent values of constant laminated shale volume, V_{lam}. Note that resolution becomes degraded for values of V_{lam} greater than 0.5.

Figure 11 presents the anisotropic interpretation of the test well MCI data. Track 1 represents the resistivity. Because there is zero relative dip, the horizontal resistivity, shown in blue, overlays the deep induction resistivity, shown in red. The light blue cyan curve is the vertical resistivity and the orange curve is the interpreted sand resistivity. Track 2 represents the lithology, dark green representing clay, light green silt and yellow sandstone. In this track, the dispersed shale-bound water is orange, the laminated shale-bound water is light blue, and the free water is dark blue. Track 3 represents the neutron and density porosity logs. Track 4 represents the volume of laminated shale (green) from the MCI anisotropic interpretation and the volume of dispersed shale (purple) computed from the difference of a shale volume computed from a gamma ray minus the volume-laminated shale. Note here that the volume of dispersed shale is inconsistent with the Thomas-Stieber model, which states that the maximum dispersed shale must be less than the shale porosity (about 6pu). Thus, there is an inconsistency between the externally supplied shale volume, MCI-computed laminated shale volume, and the Thomas-Stieber model, which need to be resolved but will not be here because of a lack of geological data. Note that below approximately 1,800 ft, where there is a lot of laminated shale, the sand resistivity becomes noisy for data near the pure shale point as discussed above.

Additional LWD and Wireline Field Examples will be presented at the AAPG Singapore conference subject to acquiring data release forms from the operators.

Conclusions

This paper provided a complete rock model and a comprehensive workflow that takes into account all the necessary stages to estimate water saturation in a thinly bedded sand-shale sequence, where both laminated and dispersed shale types can exist and anisotropic resistivity data is available.

A comparison between the Thomas-Stieber model and the anisotropic resistivity model has been made. It has been shown that these models can be equivalent when there is no relative dip. When there is dip, both models can be equivalent if: 1) that relative dip is known or available from image data, 2) that we have a pure shale zone, and 3) that the anisotropy coefficient, λ^2, is known in the pure shale.

A net-pay flag dependent on formation effective porosity, ϕ_e, can be expected to find less pay (cumulative footage) then that found with a net-pay flag dependent on sand effective porosity, $\phi_{e\text{-}sd}$, even though the volume of the hydrocarbon in the formation is the same for both cases.

Charts have been constructed showing how the MCI horizontal, R_h, vertical, R_v, and deep induction, R_{log}, resitivities vary as a function of laminated shale volume and dip.

Wireline/LWD tools sensitivities to dip and anisotropy have been presented. It has been shown that "geosteering tools" can be used for an anisotropic interpretation as long as the relative dip is greater than 40°. The newer LWD and wireline anisotropic tools are suitable for anisotropy interpretation at any relative dip.

The basic acquisition, processing and interpretation principles of a new wireline anisotropic tool have been summarized.

An example from a test well has been presented demonstrating the sensitivity of the anisotropic resistivity model to the input parameters. The model is particularly sensitive to minor data perturbations near the "pure shale point".

References

Hayden, R., A. Kosten, S. Jacobson, J. Grant, S. Alderman, B. Katon, C.B. Liu, K. Schwartz, and T. Pham, 2009, Thin Bed Interpretation Techniques for Northwestern Gulf of Mexico Coastal and Offshore Clastics: 2009 SPWLA Annual Symposium, Houston, Texas.

Hou, J., L. San Martin, D. Wu, F.T. Celepcikay, and D. Torres, 2012, Real Time Borehole Correction for a New Multi-Component Array Induction Logging Tool in OBM Wells: SPWLA 53rd Annual Logging Symposium, Cartegena, Columbia, 16–20 June.

Klein, J.D., P.R. Martin, and D.F. Allen, 1997, The Petrophysics of Electrically Anisotropic Reservoirs: 1995 SPWLA Annual Logging Symposium.

Minh, C.C., J. Clavaud, P. Sundararaman, S. Froment, E. Caroli, O. Billon, G. Davis, and R. Fairbairn, 2008 Graphical Analysis of Laminated Sand-Shale Formations in the Presence of Anisotropic Shales: Petrophysics, v. 49/5, p. 395–405.

Mollison, R.A., O.N. Fannini, L. Kriegshauser, L. Yu, G. Ugueto, and J. van Popta, 2001, Impact of Multi-component Induction Technology on a Deepwater Turbidite Sand Hydrocarbon Saturation Evaluation: 2001 SPWLA Annual Logging Symposium, Houston, Texas.

Moran, J.H., and S. Gianzero, 1979, Effects of Formation Anisotropy on Resistivity-Logging Measurements: Geophysics, v. 44/7, p. 1266-1286.

Thomas, E., and S. Stieber, 1975, The Distribution of Shale in Sandstones and its Effect upon Porosity: 16th SPWLA Annual Logging Symposium.

Yared, K., M. Pelorosso, I. Altintutar, D. Buster, E. Manuel, J. Doyle, and C. Russell, 2010, Novel Approach to Quantifying Deepwater Laminated Sequences Using Integrated Evaluation of LWD Real-Time Shear, Porosity, Azimuthal Density and High-Resolution Propagation Resistivity: Deepwater Drilling and Completion Conference, Galveston, Texas, 5–8 October 2010. SPE paper 134515.

Yin, Y., and B. Kurniawan, 2008, Resistivity Anisotropy Models and Multi-Component Induction Measurements: Impact on Sw and Uncertainty of PPV Estimation: 2008 SPWLA Annual Symposium, Paper LLLL

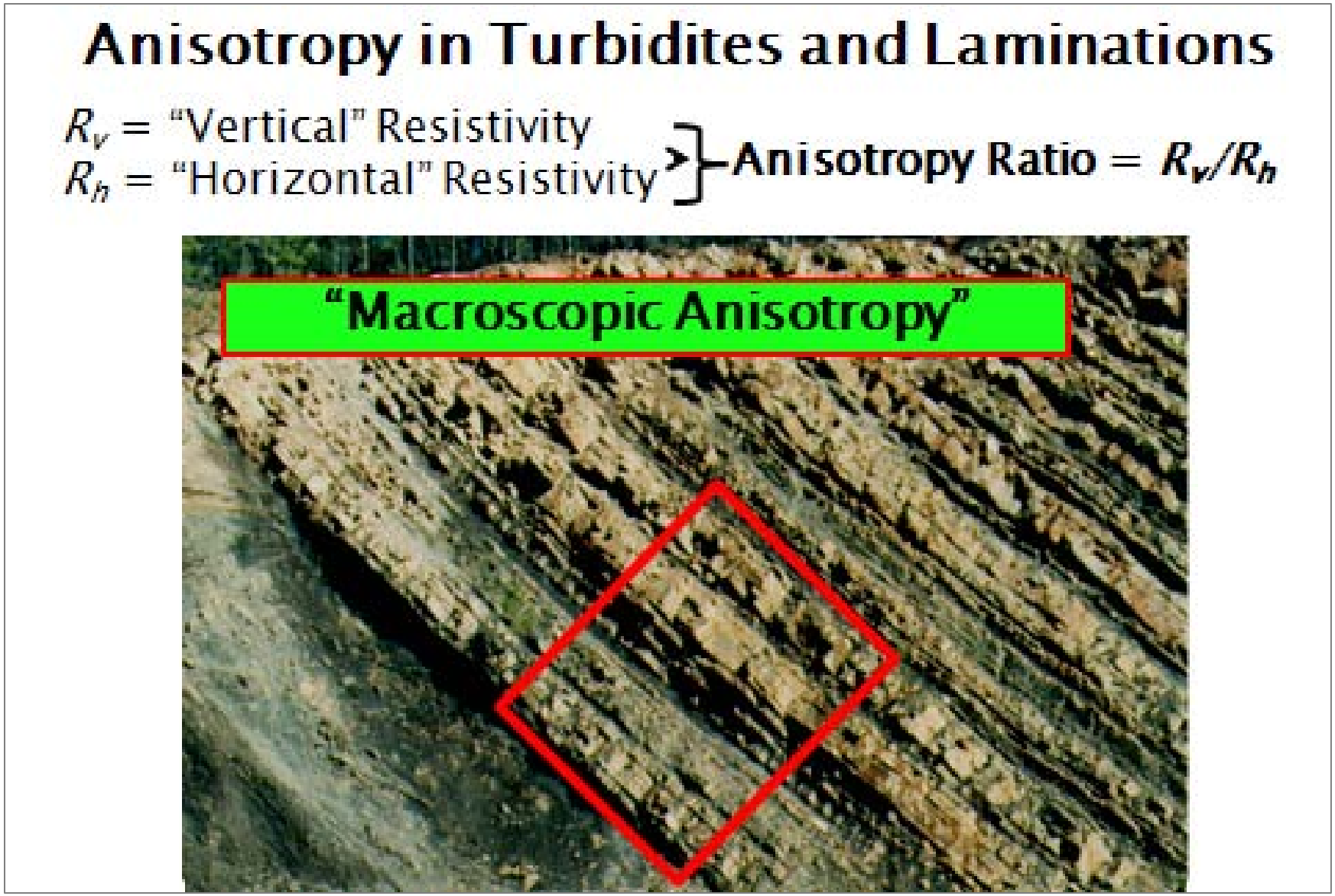

Figure 1. Illustration of the Macro Anisotropy concept.

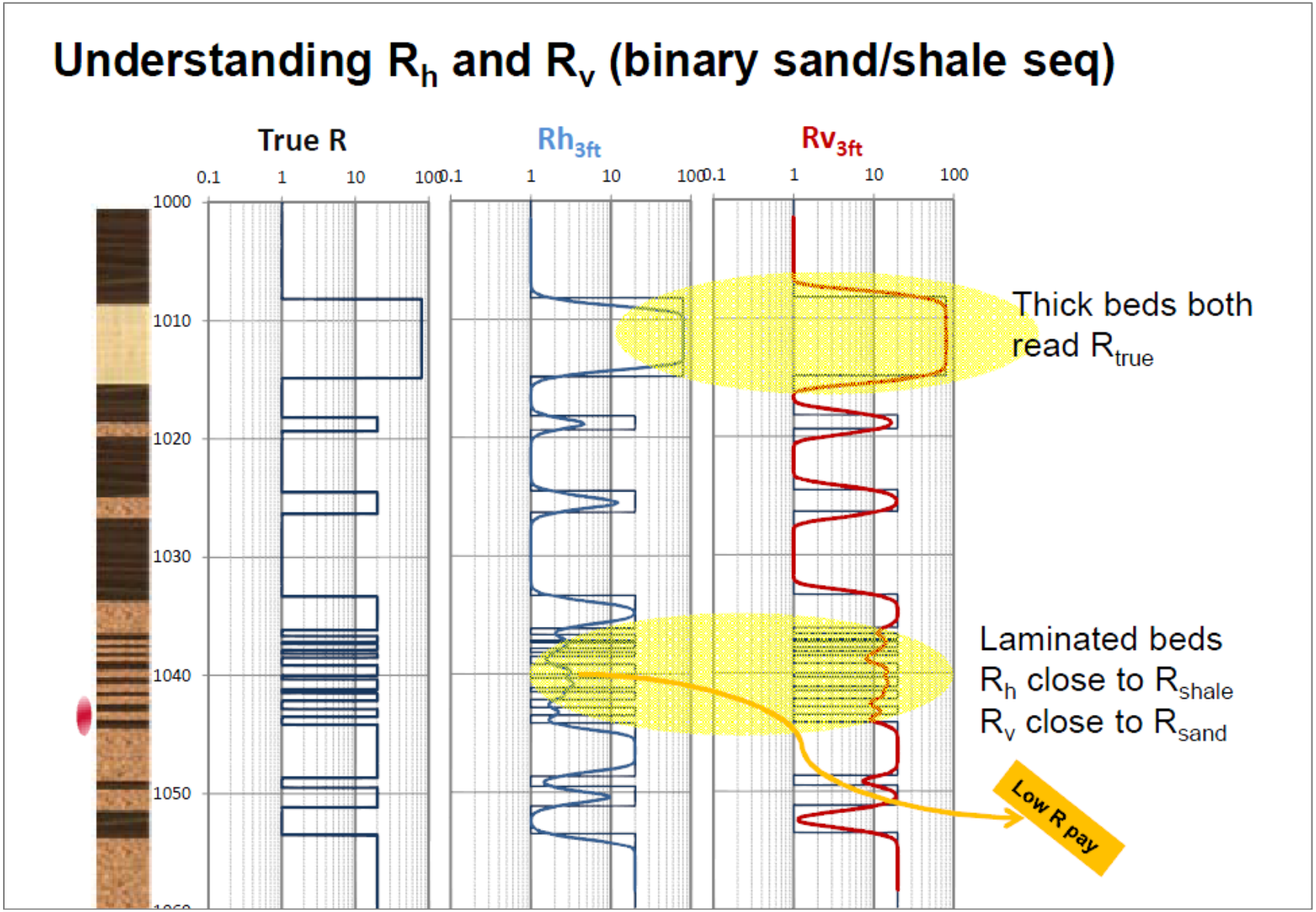

Figure 2. Simulated data illustrating the effect of laminated beds and Macro Anisotropy on resistivities, R_h and R_v.

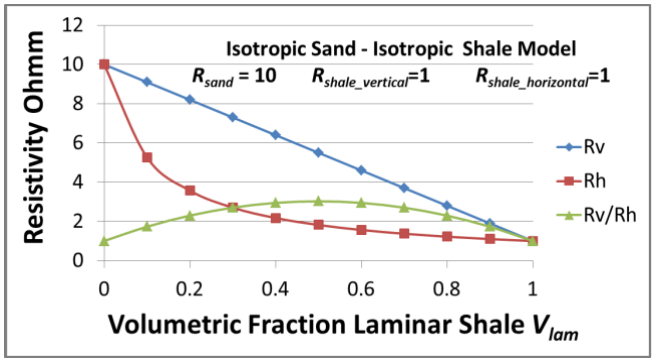

Figure 3a. Isotropic sand – Isotropic shale model.

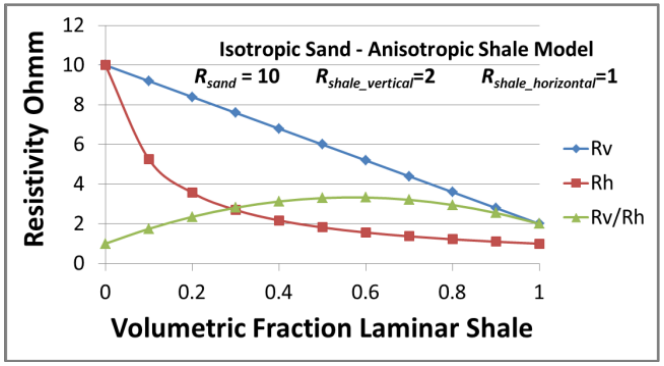

Figure 3b. Isotropic sand – anisotropic shale.

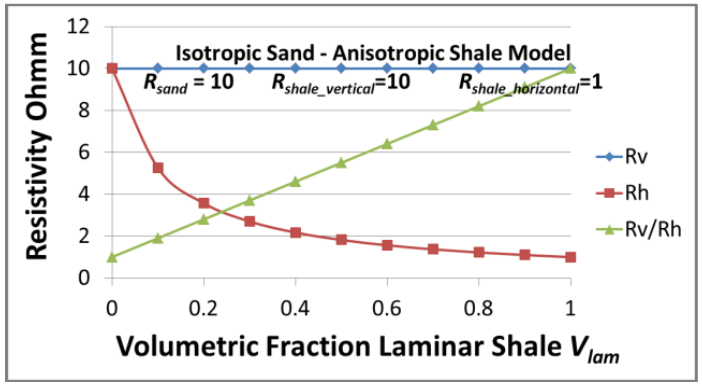

Figure 3c. Isotropic sand – strongly anisotropic shale.

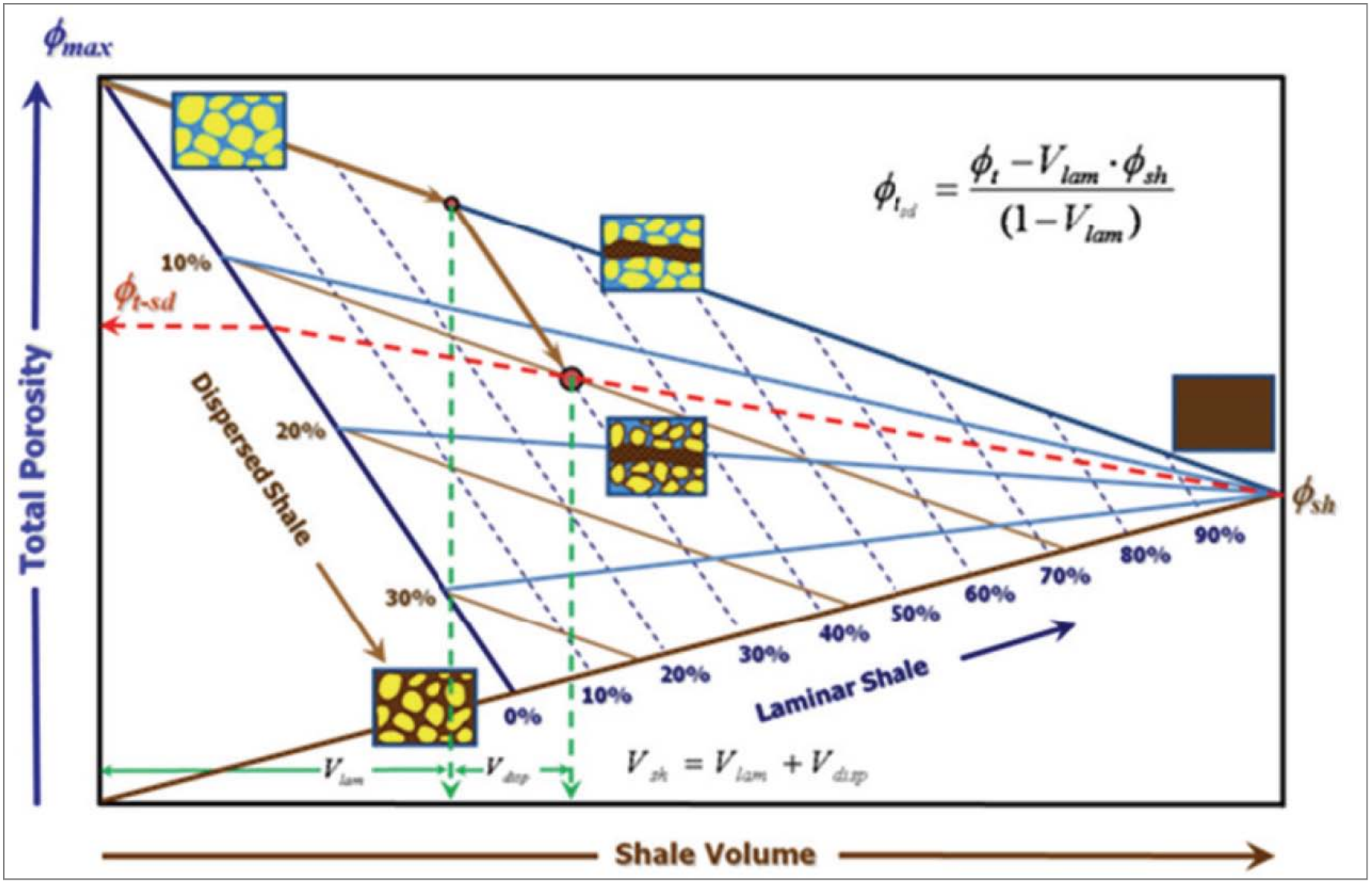

Figure 4. Thomas-Stieber shale distribution model and the graphical representation of sand porosity (from Yared et al. 2010).

Thomas-Stieber Interpretation	Anisotropy-Based Interpretation
Input volume shale, total porosity and R_t	Input volume shale, total porosity and R_v and R_h
Output volume laminated shale, dispersed shale and sand total porosity	Output volume laminated shale, dispersed shale, sand resistivity and sand total porosity
With zero dip, sand resistivity can also be obtained	
Cut-off criteria: volume laminated shale, sand effective porosity and possibly saturation	Cut-off criteria: volume laminated shale, sand effective porosity and possibly sand water saturation

Figure 5. Comparison of Thomas-Stieber interpretation with resistivity-based anisotropic interpretation.

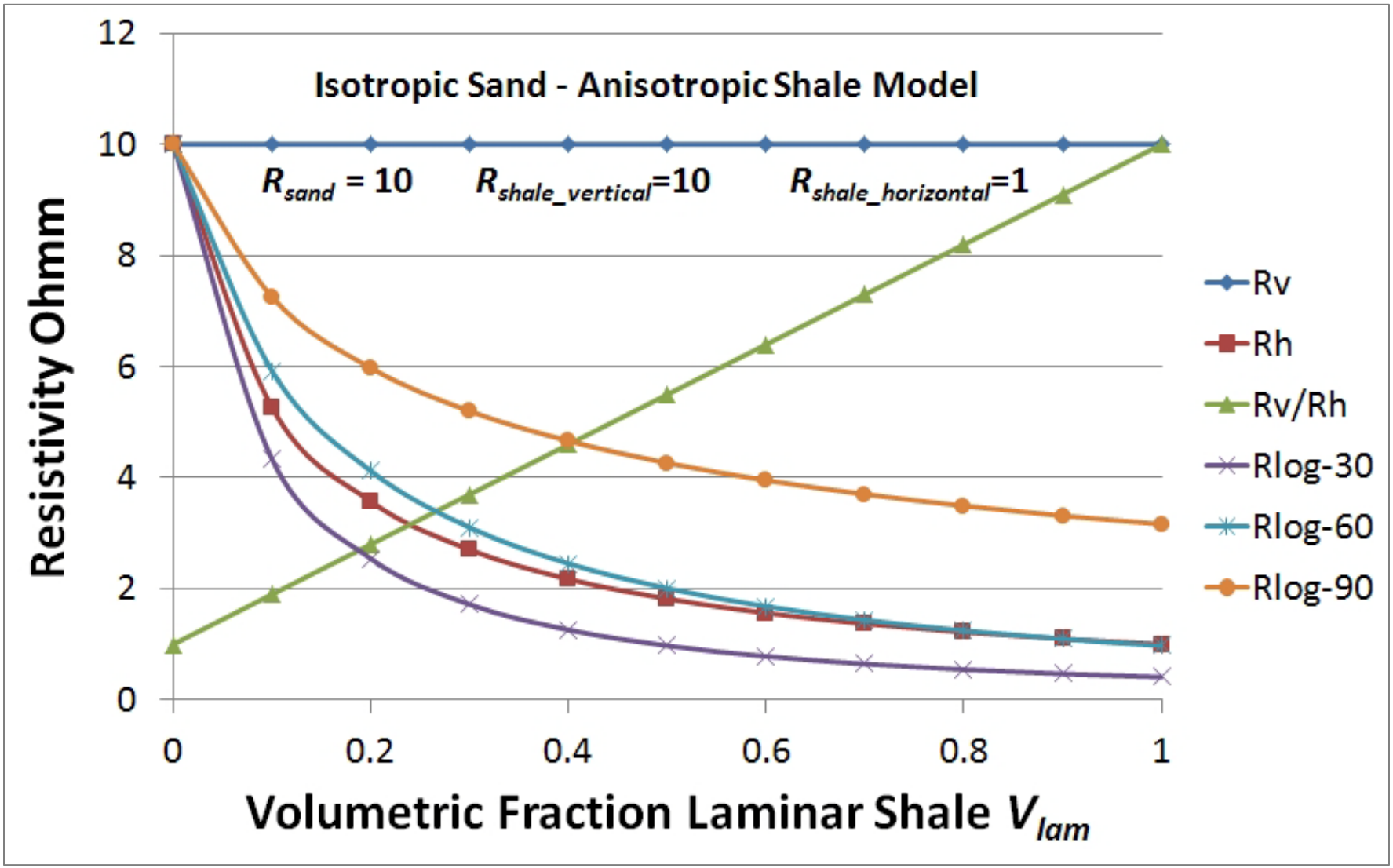

Figure 6. Sensitivity of the measured resistivity, Rlog, to Relative Dip in a highly-anisotropic formation (Shale $\lambda^2 = 10$).

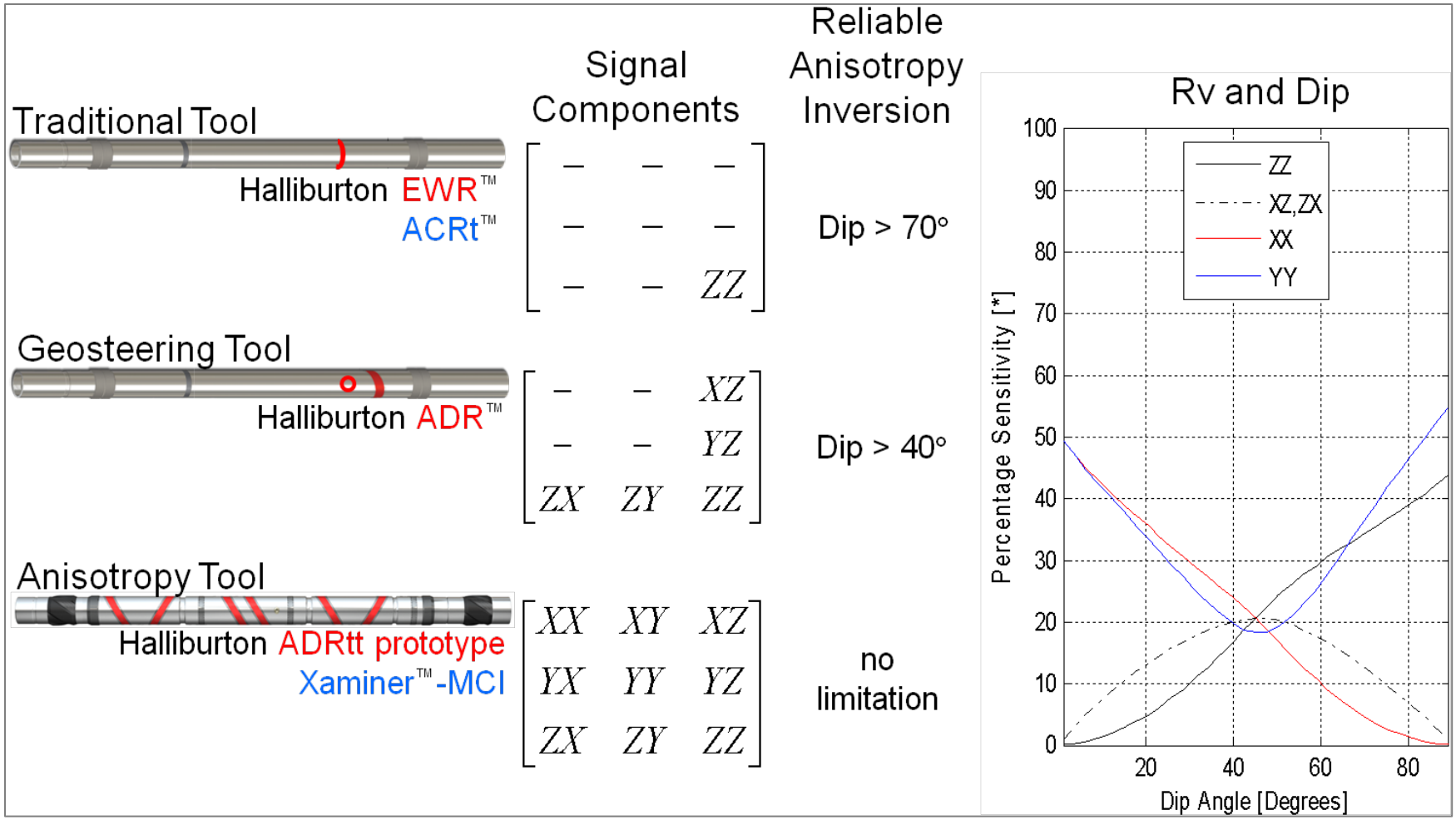

Figure 7. Different resistivity tool types and sensitivity to anisotropy and intrinsic dip.

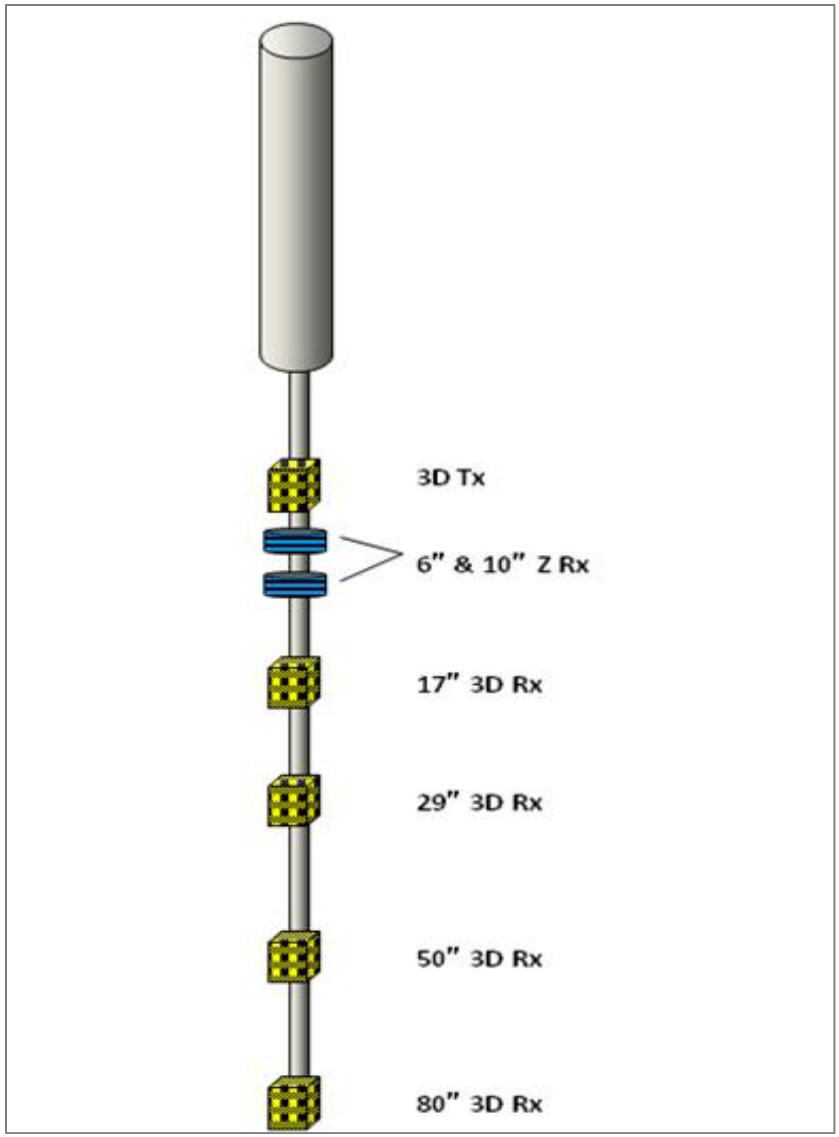

Figure 8. Configuration of Halliburton's Xaminer™-MCI tool

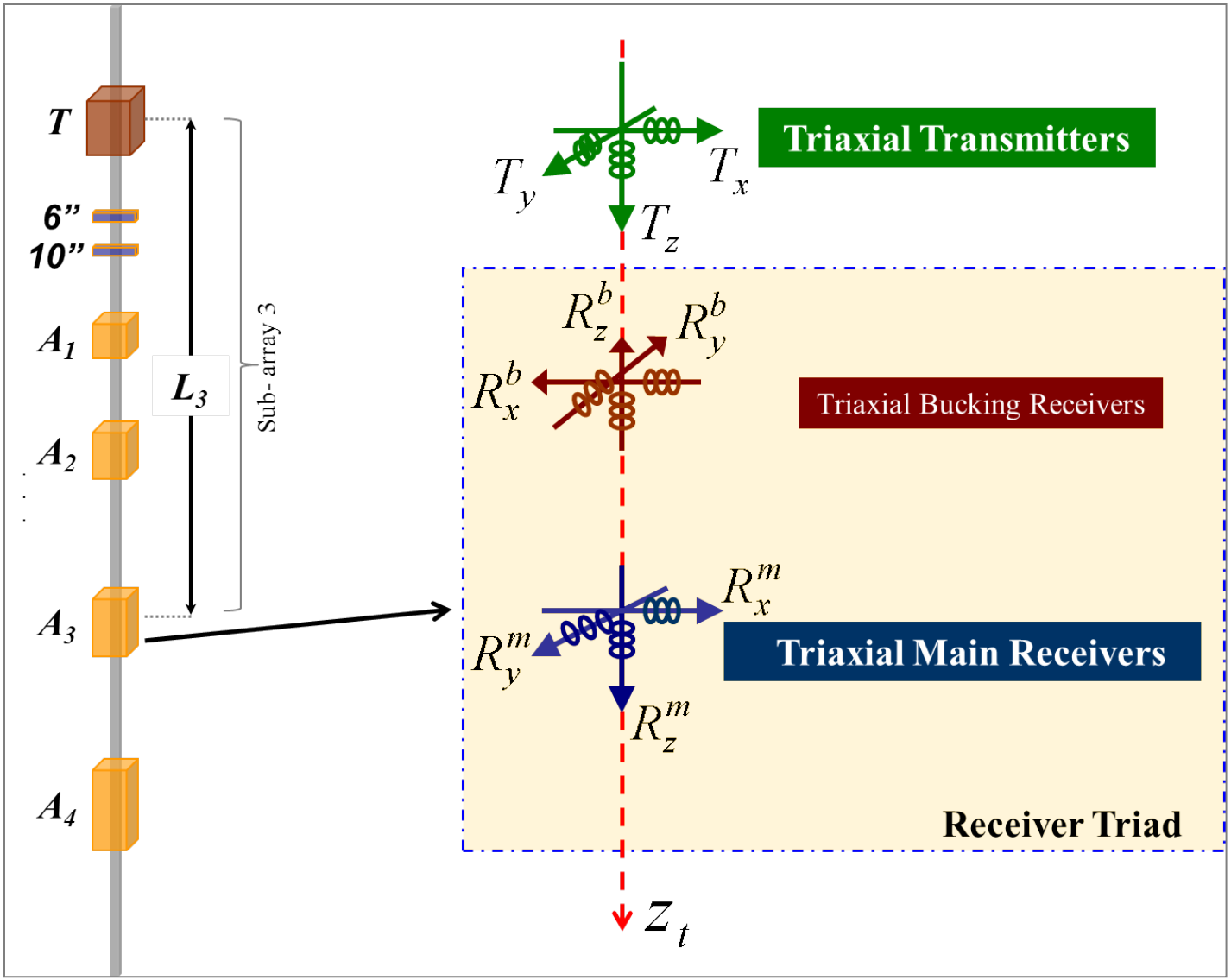

Figure 9. Diagram of a multi-triad triaxial induction array showing configuration and its equivalent dipole model (for one triad) in the tool/measurement coordinate system (x_t, y_t, z_t). L_m is the spacing between transmitter and main receiver coils (from Hou et al. 2012).

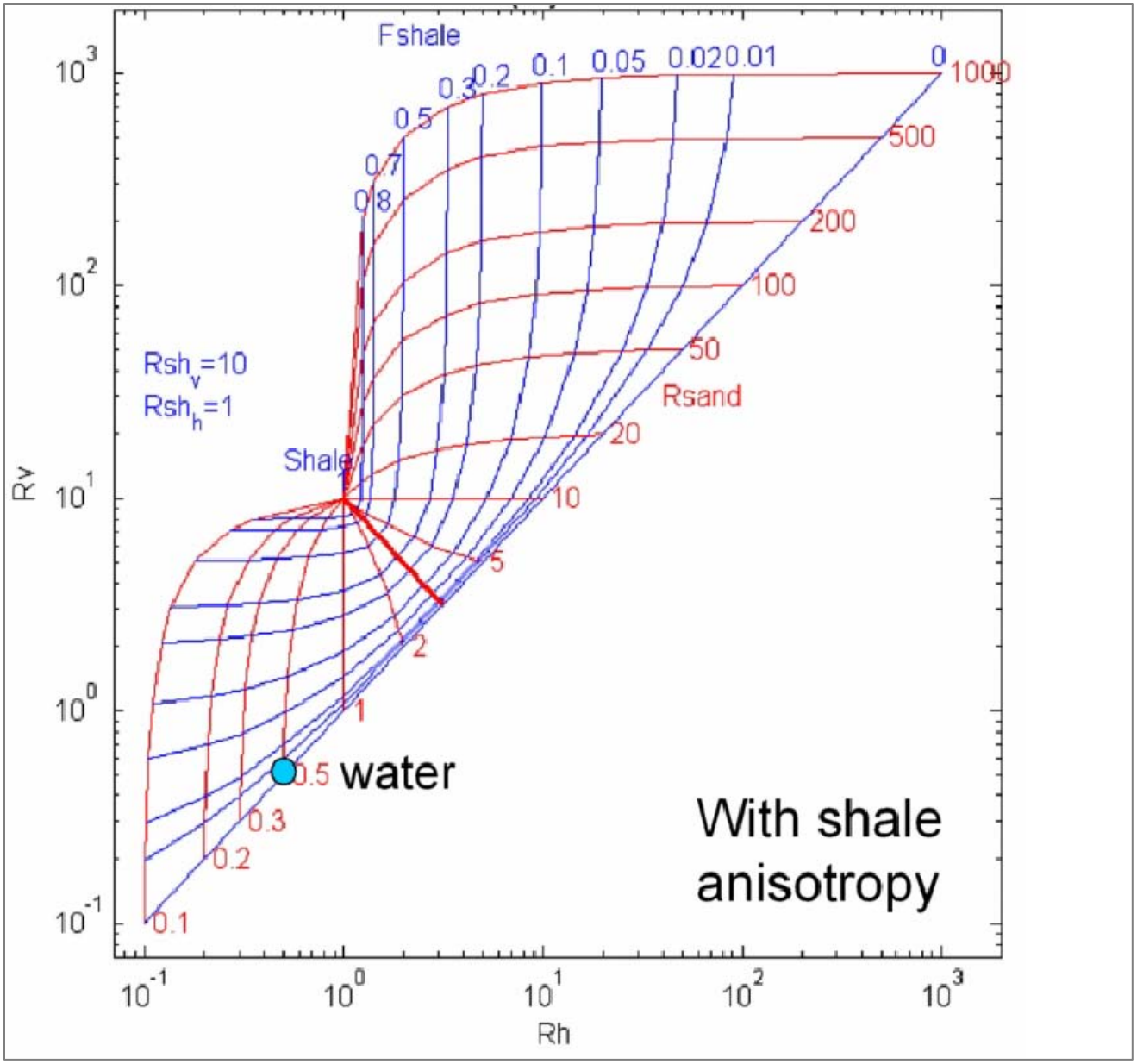

Figure 10. Graphical representation of the solutions to Eqs. 1–3 for $R_{shale\_vertical} = 10$ and $R_{shale\_horizontal} = 1$ (From Minh et al 2008).

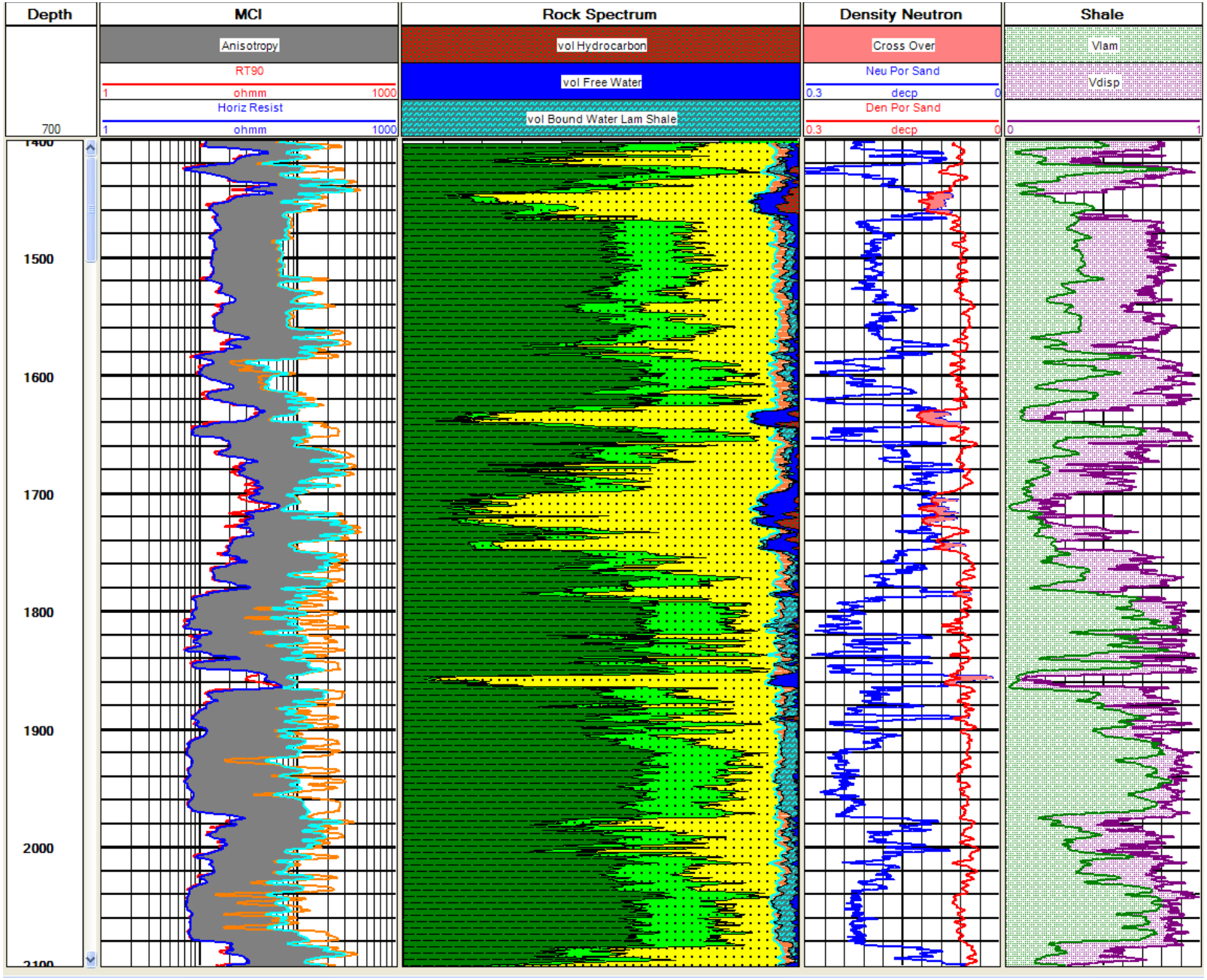

Figure 11. Anisotropic model interpreted results from the Fort Worth, Texas test well.